Solar Physics
DOI: 10.1007/•••••-•••-•••-••••-•

How to optimize nonlinear force-free coronal magnetic field extrapolations from SDO/HMI vector magnetograms?

T. Wiegelmann [1] · J.K. Thalmann [1] · B. Inhester [1] · T. Tadesse [1,3] · X. Sun [2] · J.T. Hoeksema [2]

© Springer ••••

Abstract
The SDO/HMI instruments provide photospheric vector magnetograms with a high spatial and temporal resolution. Our intention is to model the coronal magnetic field above active regions with the help of a nonlinear force-free extrapolation code. Our code is based on an optimization principle and has been tested extensively with semi-analytic and numeric equilibria and been applied before to vector magnetograms from Hinode and ground based observations. Recently we implemented a new version which takes measurement errors in photospheric vector magnetograms into account. Photospheric field measurements are often due to measurement errors and finite nonmagnetic forces inconsistent as a boundary for a force-free field in the corona. In order to deal with these uncertainties, we developed two improvements: 1.) Preprocessing of the surface measurements in order to make them compatible with a force-free field 2.) The new code keeps a balance between the force-free constraint and deviation from the photospheric field measurements. Both methods contain free parameters, which have to be optimized for use with data from SDO/HMI. Within this work we describe the corresponding analysis method and evaluate the force-free equilibria by means of how well force-freeness and solenoidal conditions are fulfilled, the angle between magnetic field and electric current and by comparing projections of magnetic field lines with coronal images from SDO/AIA. We also compute the available free magnetic energy and discuss the potential influence of control parameters.

Keywords: Active Regions, Magnetic Fields; Active Regions, Models; Magnetic fields, Corona; Magnetic fields, Photosphere; Magnetic fields, Models

[1] Max-Planck-Institut für Sonnensystemforschung,
Max-Planck-Strasse 2, 37191 Katlenburg-Lindau, Germany
email: wiegelmann@mps.mpg.de
[2] W.W. Hansen Experimental Physics Laboratory, Stanford University, Stanford, CA 94305, USA
[3] Addis Ababa University, College of Natural Sciences, Institute of Geophysics, Space Science, and Astronomy, Po.Box 1176, Addis Ababa, Ethiopia

arXiv:1202.3601v1 [astro-ph.SR] 16 Feb 2012

1. Introduction

The Helioseismic and Magnetic Imager (HMI) on board of the Solar Dynamics Observatory (SDO) provides us with measurements based on which the photospheric magnetic field vector can be derived (Schou *et al.*, 2010). Within this work we describe how these measurements can be extrapolated into the solar corona under the assumption that the coronal magnetic field is force-free, which means that the Lorentz-force vanishes. We compare the resulting magnetic field models with observations of the coronal plasma from the Atmospheric Imaging Assembly (AIA), which is also onboard of SDO.

The force-free field equations are given by

$$(\nabla \times \mathbf{B}) \times \mathbf{B} = \mathbf{0} \tag{1}$$

$$\nabla \cdot \mathbf{B} = 0 \tag{2}$$

subject to the boundary condition

$$\mathbf{B} = \mathbf{B}_{\rm obs} \,\text{on the bottom boundary} \tag{3}$$

where $\mathbf{B}$ is the 3D magnetic field and $\mathbf{B}_{\rm obs}$ the measured magnetic field vector in the photosphere. (Bineau, 1972; Amari, Boulmezaoud, and Aly, 2006) investigated the mathematical structure of these equations regarding existence, uniqueness and well-posedness. (Boulmezaoud and Amari, 2000) proofed the existence of force-free solutions for simple and multiple connected domains. (Aly, 2005) proofed uniqueness of force-free fields for a special cylindrical configuration. Several methods have been developed to solve these equations numerically. For reviews see (Sakurai, 1989; Aly, 1989; Amari *et al.*, 1997; Wiegelmann, 2008) and within the last few years the different numerical codes have been intensively tested, evaluated and compared in (Schrijver *et al.*, 2006; Metcalf *et al.*, 2008; Schrijver *et al.*, 2008). As result of a joint study (DeRosa *et al.*, 2009) it has been concluded that a successful application of nonlinear force free field (NLFFF) extrapolation methods require:

i) Large model volumes at high resolution, which accommodate most of the magnetic connectivity within an active region and to its surroundings.
The field of view of the isolated active region AR11158, as shown in Figs. 1 and 2, looks like a suitable candidate to fulfill this requirement.

ii) Accommodation of measurement uncertainties in the transverse field component.
This has been implemented in recent updates of different NLFFF extrapolation codes, see (Wheatland and Régnier, 2009; Wiegelmann and Inhester, 2010; Amari and Aly, 2010; Wheatland and Leka, 2011; Tadesse *et al.*, 2011b).

iii) Preprocessing of the photospheric vector field for a realistic approximation of the upper-chromospheric, nearly force-free field [1]

[1] Preprocessing of inconsistent boundary data is in particular important for methods using the magnetic field vector directly as boundary condition. Grad Rubin methods use the normal magnetic field and electric current (for one polarity) as boundary condition. The vertical current is

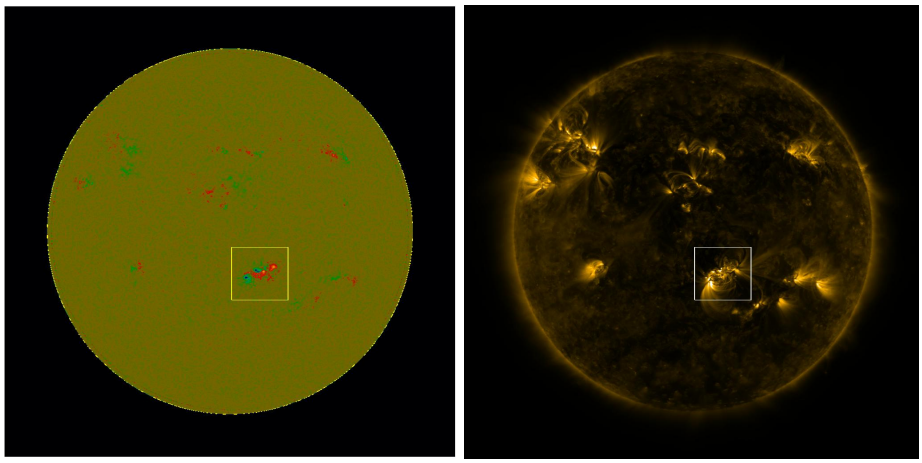

Figure 1. Left: Full disk SDO/HMI magnetogram, Right: Full disk AIA171Å image. Both data sets have been obtained on Feb. 14. 2011 at 20:34 and have been aligned as described in the SDO data analysis guide [DeRosa & Slater 2011, http://www.lmsal.com/sdouserguide.html]. The rectangle outlines the sub-region (AR11158) in the vector magnetogram which is used for the force-free field modeling.

As we will see in section 2.1 the HMI-vector magnetogram shown in Fig. 3 is almost force-free. Tools for implementing the measurement errors (previous item) can also deal with the remaining small forces. For comparison we investigate also preprocessed data.

iv) Force-free models should be compared with coronal observations.
In Figs. 5, 6 and Table 1 we compare the force-free models with coronal images observed with SDO/AIA.

2. Instrumentation and data set

The HMI instrument (Schou *et al.*, 2010) on SDO observes the full Sun at six wavelengths in the Fe I 6173 Å absorption line. Filtergrams with a plate scale of $0.5''$ pixels are collected and converted to observable quantities like Dopplergrams, continuum filtergrams, line-of-sight and vector magnetograms. For vector data, each set of filtergrams takes 135 seconds to be completed and the filtergrams are then averaged over a period of about 12 minutes. [See the HMI-hompage for details: http://hmi.stanford.edu/] To generate the vector magnetograms, Stokes parameters are derived from the averaged filtergrams and inverted with the help of a Milne-Eddington algorithm, an advanced version of the Very Fast Inversion of the Stokes Vector (VFISV) (Borrero *et al.*, 2010). The magnetic filling factor is set to be 1 in the inversion. With the amount of

derived from the transverse magnetic field and these conditions are per construction well posed, even if the photospheric magnetic field vector is not force-free. Consequently preprocessing is not crucial for these methods.

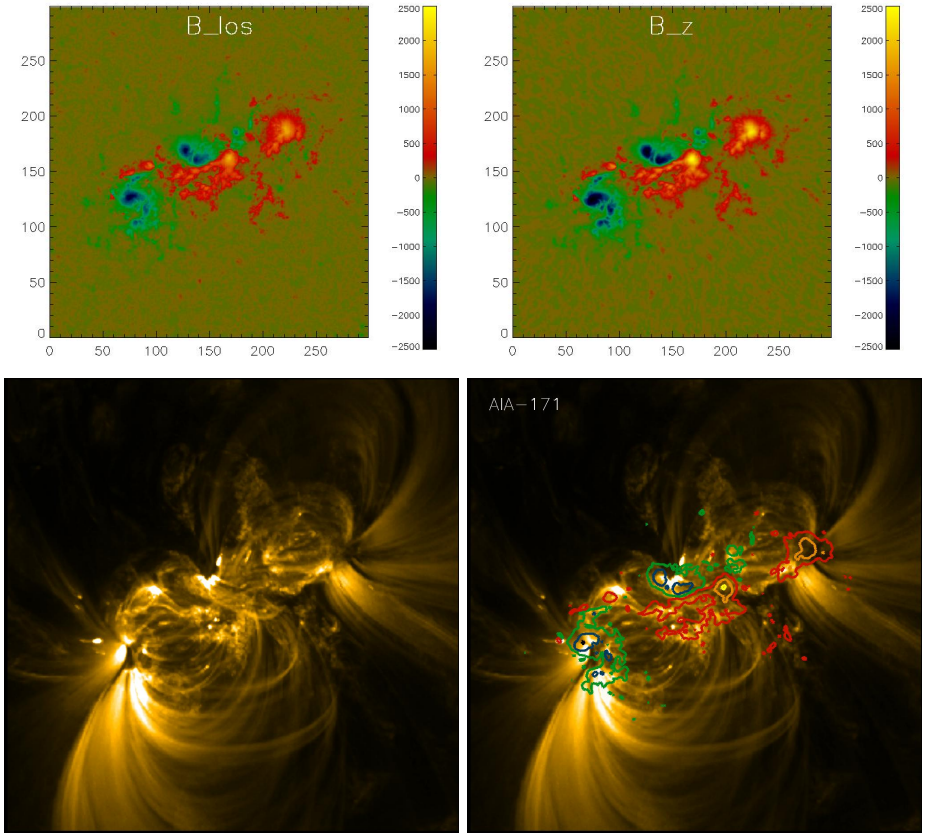

Figure 2. Top left: $B_{\rm los}$ cut from full disk HMI magnetogram. Top right: B_z from vector magnetogram. To aline the vector magnetogram with the line of sight magnetogram and AIA we carried out a correlation analysis and the correlation between $B_{\rm los}$ and B_z is 92%. Bottom: Same field of view seen in AIA171$\mathring{A}$. In the right picture we over-plotted contour lines of B_z (same color-code as in images above)

information HMI provides about the line profile, this provides the most stable results. One could determine the filling factor in strong field regions, where it is expected to be close to unity. In weak field regions, however, it is difficult to resolve the filling factor as well as field strength. The 180° azimuthal ambiguity in the transverse field is resolved by an improved version of the minimum energy algorithm (Metcalf, 1994; Metcalf *et al.*, 2006; Leka *et al.*, 2009). HMI vector field uncertainties depend on field strength, disk position, and orbital velocity. Formal uncertainties due to the inversion are computed for each pixel as part of the normal processing. Conservatively, the random errors in the line-of-sight component are about 5 G, while the uncertainty in the transverse field is as much as 200 G in weak field regions and as little as 70 G where the field is strong. The zero point uncertainty in the longitudinal direction is $< 0.1G$. Additional uncertainties arise because of the disambiguation and systematic errors that are not as well quantified.

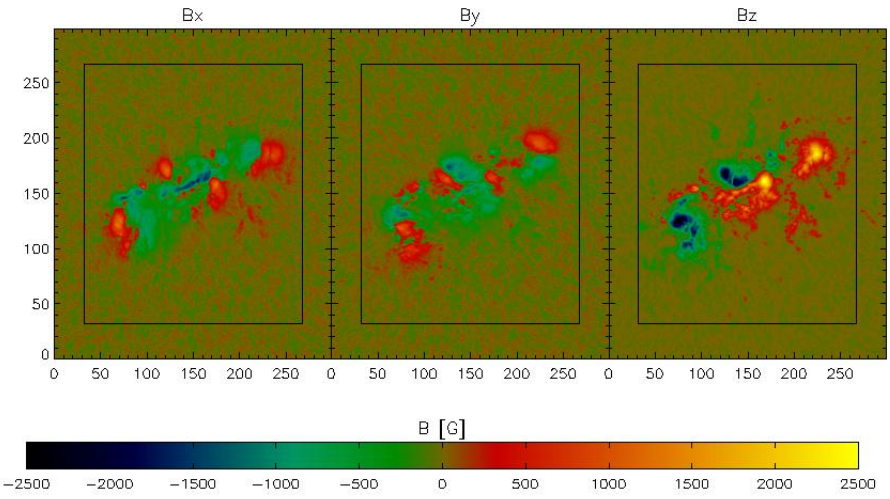

Figure 3. SDO/HMI vector magnetogram observed on Feb. 14, 2011 at 20:34UT. The rectangular area marks the inner box, where $w_f = w_d = 1$, see section 3 for details.

Regions of interest (ROIs) containing strong magnetic fluxes are automatically identified (Turmon *et al.*, 2010). Fig. 3 shows a vector magnetogram, containing AR 11158 observed on Feb. 14, 2011 at 20:34UT. After correcting for projection effects (Gary and Hagyard, 1990) the data have been mapped to a local Cartesian coordinate using Lambert equal area projection (Calabretta and Greisen, 2002). [An overview about processing of HMI vector magnetograms can be found at http://jsoc.stanford.edu/jsocwiki/VectorMagneticField/.] For the magnetic field extrapolation, we bin the data to 720 km pixel (about $1''$) and use a computational box of $300 \times 300 \times 160$ grid points.

2.1. Quality of the HMI vector magnetogram

To serve as suitable lower boundary condition for a force-free modeling, vector magnetograms have to be approximately flux balanced and the net force and net torque have to vanish. (Wiegelmann, Inhester, and Sakurai, 2006) introduced three dimensionless parameters, the flux balance ϵ_{flux}, net force balance $\epsilon_{\mathrm{force}}$ and net torque balance $\epsilon_{\mathrm{torque}}$:

$$\epsilon_{\mathrm{flux}} = \frac{\int_S B_z}{\int_S |B_z|}$$

$$\epsilon_{\mathrm{force}} = \frac{|\int_S B_x B_z| + |\int_S B_y B_z| + |\int_S (B_x^2 + B_y^2) - B_z^2|}{\int_S (B_x^2 + B_y^2 + B_z^2)}$$

$$\epsilon_{\mathrm{torque}} = \frac{|\int_S x((B_x^2 + B_y^2) - B_z^2)| + |\int_S y((B_x^2 + B_y^2) - B_z^2)| + |\int_S yB_xB_z - xB_yB_z|}{\int_S \sqrt{x^2 + y^2}\,(B_x^2 + B_y^2 + B_z^2)}$$

where the integrals in ϵ_{force} and ϵ_{torque} correspond to the Maxwell stress tensor and it's first moment, respectively (see (Molodensky, 1969; Molodensky, 1974; Aly, 1989)). For perfectly force-free consistent boundary conditions these three quantities are zero, while for real observed data this is hardly the case. For practical computations, however, it is sufficient these quantities become small, e.g. ($\epsilon_{\text{flux}}, \epsilon_{\text{force}}, \epsilon_{\text{torque}} \ll 1$). In the following table we list the values for the used HMI-data-set in the first row. All three quantities are well below unity, which gives us some confidence that the data might serve as suitable boundary condition for a force-free modeling.

Data set	ϵ_{flux}	ϵ_{force}	ϵ_{torque}
HMI, Feb.14 2011	0.0034	0.0564	0.0535
preprocessed HMI	0.0037	0.0002	0.0009
SFT Oct.26 1992	0.0854	0.6842	0.8837
Hinode Dec.12 2006	0.0167	0.2727	0.3387
SOLIS Jun.07 2007	0.0124	0.6400	0.6691

To deal vector magnetogram data being inconsistent with the force-free assumption, we developed a preprocessing routine (Wiegelmann, Inhester, and Sakurai, 2006), which derives suitable boundary conditions for force-free modeling from the measured photospheric data. Applying this procedure to HMI reduces ϵ_{force} and ϵ_{torque} further significantly (second row). It is notable that the values of about 0.05 in ϵ_{force} and ϵ_{torque} for the original HMI-vector magnetogram (first row) is significantly lower as observed for vector magnetograms from other ground based and space-born missions (rows 3-5) like the Solar Flare Telescope (SFT), Hinode and SOLIS [2]. For detailed investigations of these data-sets see (Wiegelmann, Inhester, and Sakurai, 2006; Schrijver *et al.*, 2008; Thalmann, Wiegelmann, and Raouafi, 2008), respectively.

3. Nonlinear force-free field modeling

We solve the force-free equations (1) - (3) by an optimization principle as proposed by (Wheatland, Sturrock, and Roumeliotis, 2000) and extended by (Wiegelmann, 2004; Wiegelmann and Inhester, 2010) in the form:

$$L = \int_V w_f \frac{|(\nabla \times \mathbf{B}) \times \mathbf{B}|^2}{B^2} + w_d \, |\nabla \cdot \mathbf{B}|^2 \, d^3V$$

[2]The values refer to other Active Regions and dates and the values are meant as some typical value-range for a particular instrument. It is planned to compare vector magnetograms for one particular active region and time observed with different instruments (SOLIS and HMI) and the corresponding force-free models (Thalmann et al., in preparation). Further investigations are necessary to clarify whether the good fulfillment of the force-free consistency criteria here is a property of this particular active region or if the HMI-measurements are more force-free generally.

$$+\nu \int_S (\mathbf{B} - \mathbf{B}_{obs}) \cdot \mathbf{W} \cdot (\mathbf{B} - \mathbf{B}_{obs}) d^2S \tag{4}$$

where ν is a Lagrangian multiplier which controls the injection speed of the boundary conditions. w_f and w_d are weighting functions, which are 1 in the region of interest (inner $236 \times 236 \times 128$ physical box) and drop to zero in a 32 pixel boundary layer towards the lateral and top boundaries of the full $300 \times 300 \times 160$ computational domain. $\mathbf{W}$ is a space-dependent diagonal matrix the element of which are inverse proportional to the estimated squared measurement error of the respective field component. In principle one could compute $\mathbf{W}$ from the measurement noise and errors obtained from the inversion of measured Stokes profiles to field components. Until these quantities become available, a reasonable assumption is that the magnetic field is measured in strong field regions more accurately than in the weak field and that the error in the photospheric transverse field is at least one order of magnitude higher as the line-of-sight component. Appropriate choices to optimize ν and $\mathbf{W}$ for use with SDO/HMI magnetograms are investigated in this paper. For a detailed description of the current code implementation and tests we refer to (Wiegelmann, 2004) for the basic code and (Wiegelmann and Inhester, 2010) for a description and tests of slow boundary injection and the consideration of measurement errors. For the first time we combine the above described algorithm with a multiscale approach as described in (Wiegelmann, 2008). For this work we apply our code with a 3 level multiscale approach to a SDO/HMI data set with 300×300 points in x and y and extrapolate 160 pixel in hight z.

3.1. Quality of the reconstructed 3D fields

To evaluate how well the force-free and divergence-free condition are satisfied by the reconstructed 3D fields, we monitor a number of expressions, which are:

$$L_1 = \int_V \frac{|(\nabla \times \mathbf{B}) \times \mathbf{B}|^2}{B^2} \, d^3V \tag{5}$$

$$L_2 = \int_V |\nabla \cdot \mathbf{B}|^2 \, d^3V \tag{6}$$

$$\sigma_j = \left(\sum_i \frac{|J_i \times B_i|}{B_i} \right) / \sum_i J_i \tag{7}$$

$$L_{1\infty} = \sup_{\mathbf{x} \in V} |\mathbf{j} \times \mathbf{B}| \tag{8}$$

$$L_{2\infty} = \sup_{\mathbf{x} \in V} |\nabla \cdot \mathbf{B}| \tag{9}$$

where L_1 and L_2 correspond to the first and second term in equation (4), respectively, with the difference that the integral is carried out in the inner $236 \times 236 \times 128$ physical box, where $w_f \equiv w_d \equiv 1$, excluding the buffer boundary of 32 pixel towards the lateral and top boundary of the computational box. For potential and linear force-free fields the values correspond to the discretisation error. Also investigated in the inner box is the sine of the current weighted

average angle σ_j between the magnetic field and electric current (see (Wheatland, Sturrock, and Roumeliotis, 2000; Schrijver *et al.*, 2006) for details) and $L_{1\infty}$ and $L_{2\infty}$, which are the L_∞ norms for the Lorentz force and divergence, respectively.

3.2. Code setup and choice of free parameters

Before we perform nonlinear force-free extrapolations we use the vertical component B_z of the HMI-data to compute a potential and a linear force-free field ($\alpha L = 2.5,\ \alpha = 1.16 \cdot 10^{-8} m^{-1}$) with a Fourier transform method (Alissandrakis, 1981) Here, α is the linear force-free parameter ($\nabla \times \mathbf{B} = \alpha \mathbf{B}$), which is 0 for a potential field. For a linear force-free field we calculate, as suggested by (Hagino and Sakurai, 2004), an averaged value $\alpha = \sum \mu_0 J_z \mathrm{sign}(B_z) / \sum |B_z|$, where $J_z = \frac{1}{\mu_0} \left(\frac{\partial B_y}{\partial x} - \frac{\partial B_x}{\partial y} \right)$ is the vertical current in the photosphere.

For nonlinear force-free fields we minimize the functional 4, we vary the Langrangian multiplier ν and the Mask W, which we want to optimize. For cases A-H we choose $W = B_T / \max(B_T)$. This seems to be a reasonable choice as the measurement error in the transverse field is higher in weak field regions. We vary the Langrangian multiplier ν between 0.1 and 0.0001 for cases A-F. The lower the value of ν, the slower the observed boundary becomes injected, so that the code has more time to relax towards a force-free state. The computing time increases with a power law when ν decreases (Time[h] $\sim 0.013h \cdot \nu^{-0.88}$), see Fig. 4a and column ten in table 1). The relation between ν and asin(σ_j), can be be approximated also by a power law (asin(σ_j) [degree] $\sim 45.7^\circ \cdot \nu^{0.28}$), see Fig. 4b). The values for force- and divergence-freeness L_1 and L_2 are slightly higher for $\nu = 10^{-4}$ than for 10^{-3}, but the general trend is that L_1 and L_2 decrease with decreasing ν in form of a power law, $L \sim 98 \cdot \nu^{0.46}$, with $L = L_1 + L_2$, see Fig. 4c). It seems that the choice $\nu = 0.001$ is optimal, as higher values of ν correspond to worse fulfilment of all force-free consistency criteria (σ_j, L_1, L_2) and a lower ν only increases the computing time drastically, but does not or hardly improve the solution.

In cases G and H we investigate the influence of preprocessing on the result. We used a standard-preprocessing parameter set $\mu_1 = \mu_2 = 1, \mu_3 = 0.001, \mu_4 = 0.01$. These parameters control the amount of force-freeness, torque-freeness, nearness to the actually observed data and smoothing, respectively (see (Wiegelmann, Inhester, and Sakurai, 2006) for details on preprocessing). NLFFF-extrapolations have been carried out here for $\nu = 0.01$ and $\nu = 0.001$ and we find that L_1 and L_2 are smaller for extrapolations from preprocessed data. Similar as in the unprocessed case L_1, L_2, σ_j decrease with decreasing ν, while the computing time increases. The computing time for preprocessed data is about a factor of a three ($\nu = 0.01$) or two ($\nu = 0.001$) higher compared with the unprocessed cases. The angle between magnetic field and current asin(σ_j) does not improve, however, and becomes worse (factor 1.3) for $\nu = 0.001$. A reason for the L-values becoming lower, while σ_j remains the same, might be that some strong current-peaks are smoothed out by preprocessing. If we consider that without preprocessing (case E) L_1 and L_2 are already of the order of the discretisation error of the potential field, the lower value σ_j and the shorter

computing times, we conclude that preprocessing is not necessary for this data set.

In the cases I-L we investigate the effect of different mask-functions. We choose a unique mask in cases I and J, which means that we do not consider different errors in high and low field strength regions in the photospheric vector magnetogram. As one can see (in comparison with cases B and E) all three force-free consistency criteria are worse and consequently one should not use a unique mask. Interesting are the cases K and L, where we choose the mask $W = (B_T/\max(B_T))^2$. This choice gives more weight to strong than to weak regions, similar as in the linear cases A-H, but prefers strong regions significantly more. For $\nu = 0.01$ (case K compared with B) L_1 and L_2 are better and σ_j worse. For $\nu = 0.001$ (case L compared with E) all three criteria are fulfilled somewhat better for the quadratic mask function. The computing time is, however, a factor of 1.6 longer for the quadratic case (L). We conclude, that if ν is sufficiently low, than the final equilibrium is quite robust regarding the exact choice of the mask function profile.

For comparison we also extrapolated the magnetogram with the old code version, which uses a fixed lower boundary and does not contain a mask and Lagrangian multiplier (cases M and N without and with preprocessing, respectively). Without preprocessing, all three force-free consistency criteria are fulfilled worse as for the new code, because the old code has no possibility to correct for inconsistencies in the magnetograms. Preprocessing improves the result for L_1 and L_2 by about a factor of four, but σ_j hardly improves. The computing time for the old code (case N) is, however, significantly lower (factor of 5, 9 compared with E,L, respectively) as for the best runs with the new code. If we compare results of the old code (case N, after preprocessing) with results from the new code with similar computing times (cases C and G) the performance are similar. Higher computing times are the price we have to pay to get better force-free consistent equilibria.

In column nine in Table 1 we present the ratio of the total magnetic energy to the energy of a potential field E/E_0. While the correct value is a priori unknown, this criteria cannot serve directly as a quality measure of the reconstructed NLFFF-fields, except that E/E_0 should be greater than unity. E/E_0 is an important quantity, as it defines an upper limit for the free magnetic energy, which could become converted in kinetic and thermal energy during eruptions. Taking the average of all 14 NLFFF-models we find $E/E_0 = 1.20 \pm 0.06$, and if we consider only the best cases, say where $\mathrm{asin}(\sigma_\mathrm{j}) < 10^\circ$ (cases D,E,F,H,J,L) one finds $E/E_0 = 1.24 \pm 0.03$. For long time series it will probably not be possible to extrapolate all magnetograms with several different parameter sets, but we propose to do this for a some magnetograms within a time series to derive an error-estimation for E/E_0. We find that this quantity is not significantly influenced by the chosen parameter set (value of Lagrangian multiplier ν, mask function profile W, preprocessing) if the force-free consistency criteria L_1, L_2, σ_j are fulfilled and one should check them for each extrapolation from vector magnetograms. We find that the L_∞ norms for Lorentz force and divergence behave very similar as the integral forms. Therefore both norms can alternatively be used to evaluate the quality of the extrapolated field.

Table 1.: Evaluation of force-free field models. The first column names the model and in column 2 and 3 are shown the used model parameters. Column 4-8 show different force-free consistency evaluations, column 9 the magnetic energy compared with a potential field and column 10 the computing time on one processor. Finally, in the last three column we compare magnetic field lines in different regions (denoted red, white, green also in Fig. 6) with an AIA-image.

Data set	ν	Mask	L_1	L_2	$\sin^{-1}\sigma_j$	$L_{1\infty}$	$L_{2\infty}$	E/E_0 [a]	Time	AIA-red	AIA-white	AIA-green
pot. field			2.0	1.9	52.5°	1198	239	1.00		473 ± 66	265 ± 9	754 ± 102
LFF α2.5			1.9	1.8	19.3°	1312	220	1.04		898 ± 270	241 ± 5	858 ± 163
A) NLFFF	0.1	$\propto \lvert B_T \rvert$	17.4	10.8	22.4°	3682	472	1.14	8min	165 ± 13	207 ± 4	645 ± 75
B) NLFFF	0.01	$\propto \lvert B_T \rvert$	10.7	4.9	14.0°	3545	356	1.17	30min	185 ± 11	211 ± 9	451 ± 86
C) NLFFF	0.005	$\propto \lvert B_T \rvert$	7.6	3.0	11.0°	3013	312	1.20	1h:22min	200 ± 9	216 ± 18	411 ± 40
D) NLFFF	0.002	$\propto \lvert B_T \rvert$	3.8	1.4	7.5°	2004	247	1.23	2h:49min	213 ± 11	232 ± 20	398 ± 28
E) NLFFF	0.001	$\propto \lvert B_T \rvert$	2.5	1.0	5.7°	1769	210	1.25	5h:46min	233 ± 16	221 ± 5	425 ± 35
F) NLFFF	0.0001	$\propto \lvert B_T \rvert$	2.8	1.1	3.5°	1771	209	1.26	51h:32min	244 ± 23	209 ± 35	432 ± 67
G) Prepro	0.01	$\propto \lvert B_T \rvert$	3.5	1.5	14.0°	1020	126	1.25(1.22)	1h:33min	207 ± 22	234 ± 12	429 ± 41
H) Prepro	0.001	$\propto \lvert B_T \rvert$	1.2	0.4	7.6°	736	70	1.28(1.24)	10h:06min	234 ± 29	285 ± 18	384 ± 27
I) NLFFF	0.01	1	19.6	8.3	17.7°	3682	438	1.10	24min	167 ± 9	204 ± 12	550 ± 86
J) NLFFF	0.001	1	13.0	5.7	8.7°	2593	330	1.18	3h:30min	201 ± 18	215 ± 24	313 ± 54
K) NLFFF	0.01	$\propto B_T^2$	7.0	4.7	14.6°	2317	324	1.08	9min	171 ± 8	201 ± 7	499 ± 95
L) NLFFF	0.001	$\propto B_T^2$	1.7	0.8	4.7°	1656	187	1.24	9h:13min	267 ± 13	206 ± 17	449 ± 53
M) Old code			27.3	11.5	16.9°	4591	581	1.15	46min	169 ± 13	209 ± 15	598 ± 75
N) Old code, preprocessed			6.5	2.9	16.6°	1196	185	1.20(1.17)	1h:02min	194 ± 25	239 ± 7	525 ± 98

[a]Preprocessing smoothes also somewhat the vertical magnetic field component and the energy of a corresponding potential field is 3% lower as for computations from the unprocessed B_z. We provide also the ratio to the original potential field in brackets for these cases.

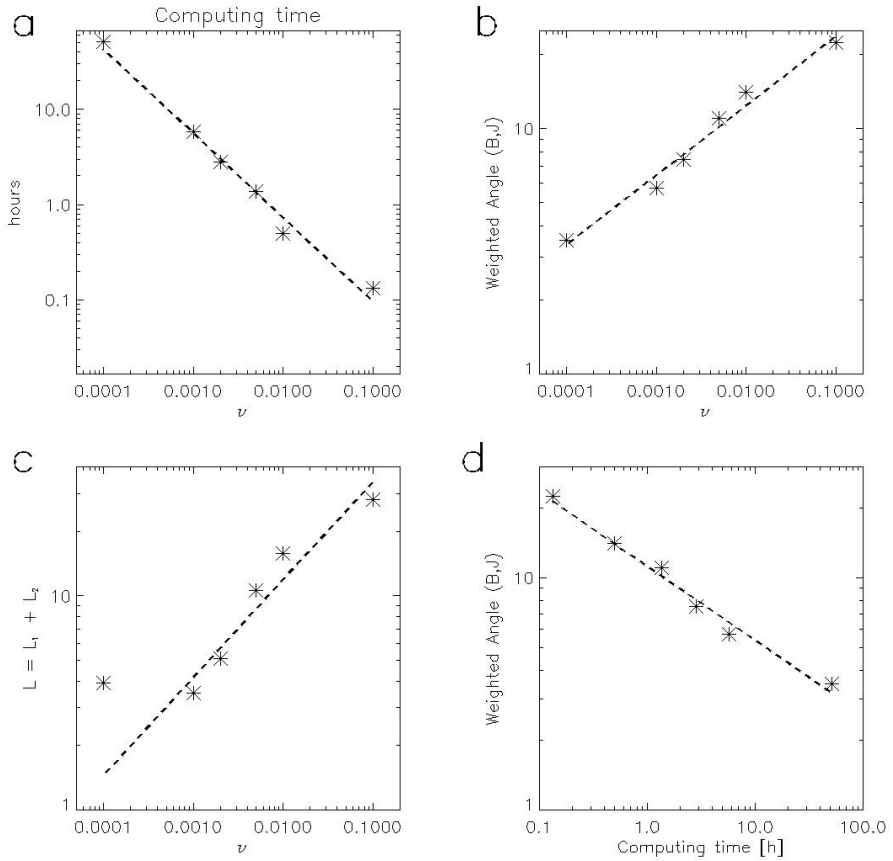

Figure 4. Relation between the Lagrangian multiplier ν and computing time (panel a), $\sin^{-1}\sigma_j$ (panel b), $L = L_1 + L_2$ (panel c). Panel d shows the relation of computing time in hours to $\sin^{-1}\sigma_j$. The values correspond to NLFFF-cases A-F in Table 1. The dashed lines show power law fits in all panels (in panel c the lowest value $\nu = 0.0001$ has been excluded for the power law fit.)

4. Comparison with AIA-images

As pointed out in (DeRosa *et al.*, 2009) force-free field models should be compared with coronal observations in order to quantify to which extend they correctly reproduce the coronal magnetic field configuration. In Fig. 5 we show some arbitrary chosen force-free field lines (from NLFFF-model-E) in comparison with AIA-images in different wavelengths. See (Lemen *et al.*, 2011) for an overview on AIA. Qualitatively it looks like the field lines reasonably agree with the observed plasma-loops. Deviations, however, are also clearly recognizable. In the following we aim to estimate the difference between force-free field lines and plasma loops quantitatively. While stereoscopic reconstructed loops in 3D as used in (DeRosa *et al.*, 2009; Conlon and Gallagher, 2010) are not available, we compare our results with an AIA-image from one viewpoint. A basic assumption is that the plasma is frozen into the magnetic field, hence the plasma loops outline

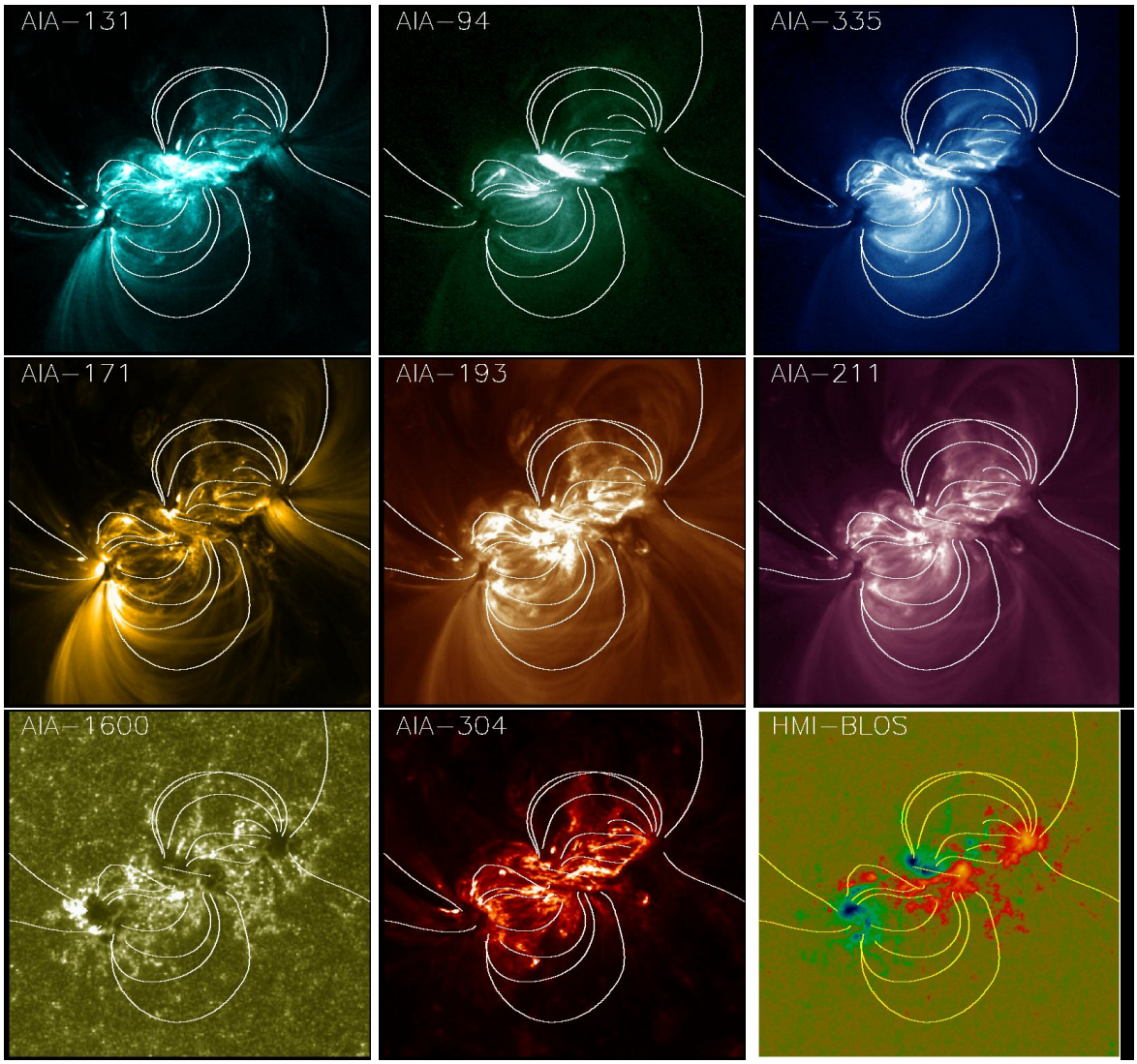

Figure 5. AIA-images of AR11158 in different wavelengths, observed on Feb. 14, 2011 at 20:34UT. Over-plotted are some selected field lines from NLFFF model E.

the magnetic field lines. Consequently, the gradient of the intensity parallel to the magnetic field lines should be small. We are interested to detect bright loops (high intensity) and to quantify the deviation of projected field lines (computed from the NLFFF-models) and plasma loops (as visible in AIA-images) as

$$C = \frac{\sqrt{\int_S (\nabla I(s))^2 ds}}{\int_S I(s) ds}, \tag{10}$$

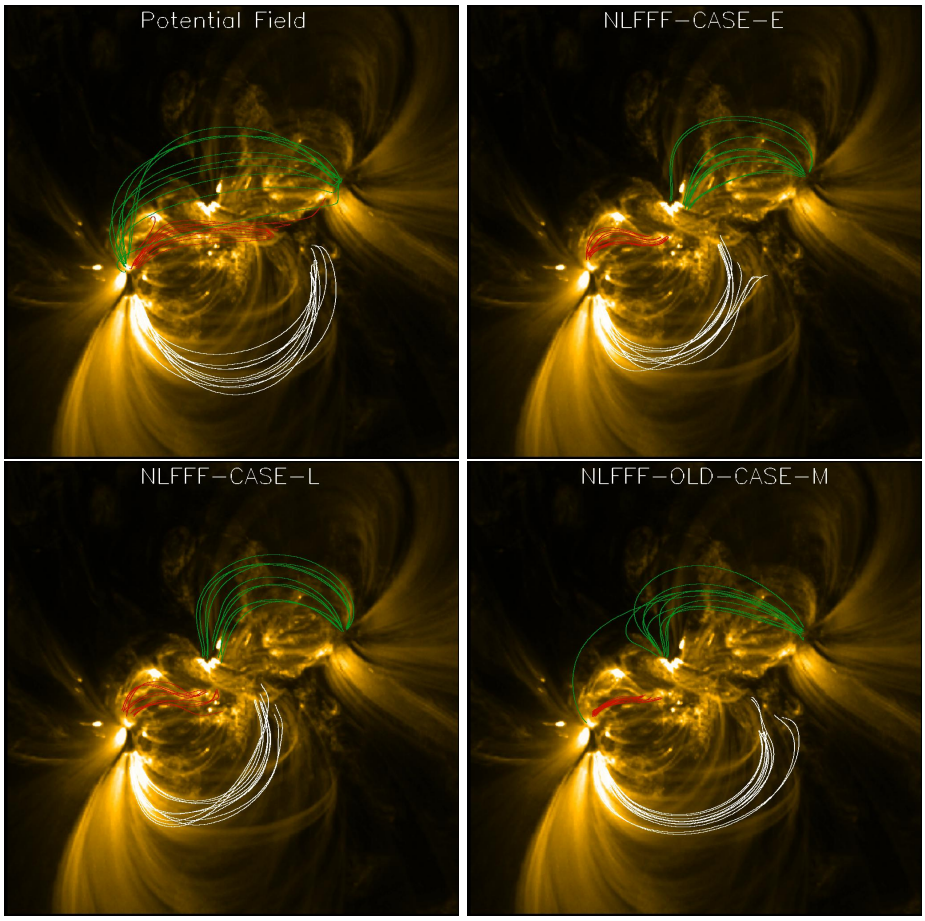

Figure 6. AIA-171 Å images with field lines as computed from selected models. The red, white and green loops here correspond to AIA-red, AIA-white and AIA-green in table 1

where $I(s)$ is the intensity along a projected magnetic field line [3]. This criterion finds loops of high $I(s)$ with small intensity gradients along the loops (low $\nabla I(s)$). For other possibilities to define the penalty function C see (Wiegelmann *et al.*, 2005; Conlon and Gallagher, 2010).

For a quantitative comparison, we compute a number of field lines, originating ± 5 pixels around previously chosen locations. These locations are $P_1 = (80, 30), P_2 = (85, 100)$ and $P_3 = (225, 185)$. Field lines not closing within the extrapolation domain are excluded from the quantitative comparison and the ten field lines owing the lowest values of C are considered for further analysis. The average and standard deviation of C for these ten field lines in each region are displayed in the last three columns of table 1, respectively. The field lines

[3]For convenience the values in last three columns in table 1 have been multiplied by 10^5 and rounded to get 3-figure integer numbers.

origination from ± 5 pixels around P_1, P_2 and P_3 are shown as red, white and green curves, respectively for some of the models in Fig. 6. The field lines corresponding to the potential field model, the NLFFF-models E and L (which best performed for the force-free consistency criteria, see last section) and a the old (fixed boundary, model M) NLFFF-code are shown in Fig. 6.

The white loops in Fig. 6 seem to agree reasonably well with AIA for all models, even those of the potential field model. The average penalty function for these loops is in the range 200-300 for all models. The red S-shaped coronal loops on the other hand cannot be identified with a potential or linear-force free model the (the linear model performing even worse than the potential one). All NLFFF-models show a much better agreement, with the penalty function for NLFFF-model (about 165-265) being in most cases less than half as large as for the potential field. The penalty function for the green loops is higher for all models, but the penalty function for the best NLFFF-models is about a factor of two better than for the potential field. It seems that these green loops are the most challenging loops to be reconstructed and the old NLFFF-code, which used a fixed boundary for the transverse potential field, performs only slightly better as the potential field. The best NLFFF-models (in the sense of most force-free, in particular cases E and L shown in Figure 6), however, indicate the correct field topology also for the green loops. Using the penalty function C to evaluate the quality of the reconstruction clearly favors NLFFF-models over potential and linear FF models. This criterion is not sensible enough, however, to definitely favor one of the NLFFF-models. In the future one should consider to sophisticate the comparison of magnetic field models with coronal images, e.g., by applying different penalty functions, use loops-structures extracted from the images and doing comparisons in different AIA-wavelengths. For some earlier observation from SDO (for which vector magnetograms have not been released yet) one could also compare the results with images taken from vantage points with one or both of the STEREO-spacecraft or compare them directly with stereoscopic reconstructed 3D-loops. This cannot, however, be implemented as a standard diagnostic for NLFFF-models, as the angle between the two STEREO spacecraft and SDO becomes to large for stereoscopy.

5. Conclusions and Outlook

Within this work we carried out nonlinear force-free coronal field extrapolations of an isolated active region based on data from SDO/HMI. The vector magnetogram is almost perfectly flux balanced and the field of view was large enough to cover also the weak field surrounding the active region. Both conditions are necessary in order to carry out meaningful force-free computations. We also found, that the photospheric magnetogram satisfied well the force-free criteria. The net force and torque are considerably smaller than in earlier measurements of other active region fields with SFT, Hinode and SOLIS. We do not know for sure, however, if this is a general property of HMI, or only true for this particular isolated active region. A comparison of an active region measurement with different instruments is planned. The data could be used

directly as boundary conditions for nonlinear force-free field computation and preprocessing the photospheric field was not necessary. The new code version incorporates errors of the measurement, in particular in the transverse field, and injects the boundary data slowly, controlled by a Lagrangian multiplier ν. The error incorporation is controlled by using a mask-function, which is 1 for the most thrustworthy data and 0 where one cannot thrust the data. Unless an exact error computation becomes available from inversion and ambiguity removal of the photospheric magnetic field vector, a reasonable assumption is that the field is measured more accurately in strong field regions and we carried out computations with the mask $\propto B_T$ and $\propto B_T^2$. For a sufficient small Lagrangian multiplier $\nu = 0.001$ we found that the resulting coronal fields are force and divergence free in the sense that the remaining residual forces are of the order of the discretisation error of potential and linear force-free fields. The weighted angle between magnetic field and electric current is about $5^\circ - 6^\circ$. The resulting field is almost identical for both masks, but computations with the $\propto B_T^2$ mask take significantly longer (9h:13min instead of 5h:46min for the $\propto B_T$ mask. Injecting the boundary faster by choosing a higher Lagrangian multiplier (say $\nu = 0.01$) speeds up the computation (to half an hour), but the residual forces are higher and current and field are not well aligned. Inserting the boundary even slower (say $\nu = 0.0001$) leads to much longer computing times (more then 50h), but does not improve the solution. We conclude that the choice $\nu = 0.001$ and a mask $\propto B_T$ or $\propto B_T^2$ are the optimal choices for this data set. The computations have been carried out on one processor on a Linux-PC. Our code has been parallelized with Open-MP, but rather then processing a single magnetogram with a parallelized code, it is planned to process different magnetograms of a time series simultaneously. While the time cadence of HMI vector magnetograms is about 12min, NLFFF computations for one magnetogram on one processor take about 6h. Consequently the requirement is about 50 processors (for each active region) in order for the NLFFF-tools to catch up with the data stream from HMI.

An important question is to which extend the optimum parameters for this data set can also be applied to other active regions from SDO/HMI. A key point is to monitor the consistency criteria of the magnetogram as well as the remaining residual forces, alignement of fields and currents in the reconstructed 3D field. A comparison of the magnetic field model with AIA-images should also always be done. We used the $171\mathring{A}$ channel here, because loops are well visible in this wavelength. The question, how coronal magnetic field models can be validated best by coronal observations should be, however, further be investigated. Magnetic field lines are 3D-structures and many field lines might not be filled with plasma and thus not visible in EUV-images. Also it is not trivial how/if one can use the different wavelength in AIA to validate coronal field models.

A stumbling stone for AR-NLFFF models could be that other active regions are not so well isolated as AR11158 investigated here, but might be magnetically connected to other ARs and the quiet Sun. Such situations require full disk vector magnetograms and force-free computations in spherical geometry, as for example carried out from full-disk SOLIS-measurements in (Tadesse *et al.*, 2011a). Due to

it's very nature extrapolations from full disk magnetograms have to be calculated with a reduced spatial resolution or one has to accept significant longer computing times. Global force-free coronal magnetic field models can also be used to specify the lateral boundaries for active region modelling for non-isolated ARs.

Acknowledgements

Data are courtesy of NASA/SDO and the AIA and HMI science teams. We are gratefully to Marc DeRosa for his help with AIA-data. This work was supported by by DLR grant 50 OC 0904 and DFG grant WI 3211/2-1.

References

Alissandrakis, C.E.: 1981, *Astron. Astrophys.* **100**, 197.
Aly, J.J.: 1989, *Solar Phys.* **120**, 19.
Aly, J.J.: 2005, *Astron. Astrophys.* **429**, 15. doi:10.1051/0004-6361:20041547.
Amari, T., Aly, J.-J.: 2010, *Astron. Astrophys.* **522**, A52. doi:10.1051/0004-6361/200913058.
Amari, T., Boulmezaoud, T.Z., Aly, J.J.: 2006, *Astron. Astrophys.* **446**, 691. doi:10.1051/0004-6361:20054076.
Amari, T., Aly, J.J., Luciani, J.F., Boulmezaoud, T.Z., Mikic, Z.: 1997, *Solar Phys.* **174**, 129.
Bineau, M.: 1972, *Comm. Pure Appl. Math.* **25**, 77.
Borrero, J.M., Tomczyk, S., Kubo, M., Socas-Navarro, H., Schou, J., Couvidat, S., Bogart, R.: 2010, *Solar Phys.*, 264. doi:10.1007/s11207-010-9515-6.
Boulmezaoud, T.Z., Amari, T.: 2000, *Zeitschrift Angewandte Mathematik und Physik* **51**, 942.
Calabretta, M.R., Greisen, E.W.: 2002, *Astron. Astrophys.* **395**, 1077. doi:10.1051/0004-6361:20021327.
Conlon, P.A., Gallagher, P.T.: 2010, *Astrophys. J.* **715**, 59. doi:10.1088/0004-637X/715/1/59.
DeRosa, M.L., Schrijver, C.J., Barnes, G., Leka, K.D., Lites, B.W., Aschwanden, M.J., Amari, T., Canou, A., McTiernan, J.M., Régnier, S., Thalmann, J.K., Valori, G., Wheatland, M.S., Wiegelmann, T., Cheung, M.C.M., Conlon, P.A., Fuhrmann, M., Inhester, B., Tadesse, T.: 2009, *Astrophys. J.* **696**, 1780. doi:10.1088/0004-637X/696/2/1780.
Gary, G.A., Hagyard, M.J.: 1990, *Solar Phys.* **126**, 21.
Hagino, M., Sakurai, T.: 2004, *Pub. Astron. Soc. Japan* **56**, 831.
Leka, K.D., Barnes, G., Crouch, A.D., Metcalf, T.R., Gary, G.A., Jing, J., Liu, Y.: 2009, *Solar Phys.* **260**, 83. doi:10.1007/s11207-009-9440-8.
Lemen, J.R., Title, A.M., Akin, D.J., Boerner, P.F., Chou, C., Drake, J.F., Duncan, D.W., Edwards, C.G., Friedlaender, F.M., Heyman, G.F., Hurlburt, N.E., Katz, N.L., Kushner, G.D., Levay, M., Lindgren, R.W., Mathur, D.P., McFeaters, E.L., Mitchell, S., Rehse, R.A., Schrijver, C.J., Springer, L.A., Stern, R.A., Tarbell, T.D., Wuelser, J.-P., Wolfson, C.J., Yanari, C., Bookbinder, J.A., Cheimets, P.N., Caldwell, D., Deluca, E.E., Gates, R., Golub, L., Park, S., Podgorski, W.A., Bush, R.I., Scherrer, P.H., Gummin, M.A., Smith, P., Auker, G., Jerram, P., Pool, P., Soufli, R., Windt, D.L., Beardsley, S., Clapp, M., Lang, J., Waltham, N.: 2011, *Solar Phys.*, 172. doi:10.1007/s11207-011-9776-8.
Metcalf, T.R.: 1994, *Solar Phys.* **155**, 235.
Metcalf, T.R., Leka, K.D., Barnes, G., Lites, B.W., Georgoulis, M.K., Pevtsov, A.A., Balasubramaniam, K.S., Gary, G.A., Jing, J., Li, J., Liu, Y., Wang, H.N., Abramenko, V., Yurchyshyn, V., Moon, Y.-J.: 2006, *Solar Phys.* **237**, 267. doi:10.1007/s11207-006-0170-x.
Metcalf, T.R., Derosa, M.L., Schrijver, C.J., Barnes, G., van Ballegooijen, A.A., Wiegelmann, T., Wheatland, M.S., Valori, G., McTiernan, J.M.: 2008, *Solar Phys.* **247**, 269. doi:10.1007/s11207-007-9110-7.
Molodensky, M.M.: 1969, *Soviet Astron.-AJ* **12**, 585.
Molodensky, M.M.: 1974, *Solar Phys.* **39**, 393.
Sakurai, T.: 1989, *Space Science Reviews* **51**, 11.
Schou, J., Borrero, J.M., Norton, A.A., Tomczyk, S., Elmore, D., Card, G.L.: 2010, *Solar Phys.*, 268. doi:10.1007/s11207-010-9639-8.
Schrijver, C.J., Derosa, M.L., Metcalf, T.R., Liu, Y., McTiernan, J., Régnier, S., Valori, G., Wheatland, M.S., Wiegelmann, T.: 2006, *Solar Phys.* **235**, 161. doi:10.1007/s11207-006-0068-7.

Schrijver, C.J., DeRosa, M.L., Metcalf, T., Barnes, G., Lites, B., Tarbell, T., McTiernan, J., Valori, G., Wiegelmann, T., Wheatland, M.S., Amari, T., Aulanier, G., Démoulin, P., Fuhrmann, M., Kusano, K., Régnier, S., Thalmann, J.K.: 2008, *Astrophys. J.* **675**, 1637. doi:10.1086/527413.

Tadesse, T., Wiegelmann, T., Inhester, B., Pevtsov, A.: 2011a, *Solar Phys.*, 236. doi:10.1007/s11207-011-9764-z.

Tadesse, T., Wiegelmann, T., Inhester, B., Pevtsov, A.: 2011b, *Astron. Astrophys.* **527**, A30+. doi:10.1051/0004-6361/201015491.

Thalmann, J.K., Wiegelmann, T., Raouafi, N.-E.: 2008, *Astron. Astrophys.* **488**, 71. doi:10.1051/0004-6361:200810235.

Turmon, M., Jones, H.P., Malanushenko, O.V., Pap, J.M.: 2010, *Solar Phys.* **262**, 277. doi:10.1007/s11207-009-9490-y.

Wheatland, M.S., Leka, K.D.: 2011, *Astrophys. J.* **728**, 112. doi:10.1088/0004-637X/728/2/112.

Wheatland, M.S., Régnier, S.: 2009, *Astrophys. J. Lett.* **700**, 88. doi:10.1088/0004-637X/700/2/L88.

Wheatland, M.S., Sturrock, P.A., Roumeliotis, G.: 2000, *Astrophys. J.* **540**, 1150.

Wiegelmann, T.: 2004, *Solar Phys.* **219**, 87.

Wiegelmann, T.: 2008, *Journal of Geophysical Research (Space Physics)* **113**(12), 3. doi:10.1029/2007JA012432.

Wiegelmann, T., Inhester, B.: 2010, *Astron. Astrophys.* **516**, A107+. doi:10.1051/0004-6361/201014391.

Wiegelmann, T., Inhester, B., Sakurai, T.: 2006, *Solar Phys.* **233**, 215.

Wiegelmann, T., Lagg, A., Solanki, S.K., Inhester, B., Woch, J.: 2005, *Astron. Astrophys.* **433**, 701.